SCIENCE CHINA
Physics, Mechanics & Astronomy

•Article•

June 2020 Vol. 63 No. 6: 264711
https://doi.org/10.1007/s11433-019-1475-8

Numerical investigation of separation-induced transition in a low-pressure turbine cascade in a low-disturbance environment

Si-Ya Jiang, and Song Fu*

School of Aerospace Engineering, Tsinghua University, Beijing 100084, China

Received September 2, 2019; accepted November 8, 2019; published online February 17, 2020

In this paper, the separation-induced transition in an LPT (low-pressure turbine) cascade is investigated at low Reynolds number with DNS (direct numerical simulation). The transition process is accurately predicted giving good agreements between the DNS and experimental results. To illustrate the secondary instability of separation-induced transition in a low-disturbance environment, the results are comprehensively analyzed in both Fourier space and physical space. It is illustrated that the effect of hyperbolic instability dominates around the saddle point of hyperbolic streamlines. This instability mechanism is responsible for the emergence of the streamwise vortices in the braid region. Elongated and intensified because of the "stretching" effect of the background flow, these vortices become the most noticeable characteristic of the flow field. Fundamental modes of small spanwise wavelength are excited in the braid region, so as some low-frequency modes. The elliptical instability plays a minor role than hyperbolic instability. It is also observed that the fundamental mode with a larger spanwise wavelength is unstable in the vortex core which is associated with the deformation of the vortex core via elliptical instability. There is no convincing evidence for the existence of subharmonic instability.

separation, direct numerical simulation, transition to turbulence

PACS number(s): 47.20.Ib, 47.27.Cn, 47.27.ek

Citation: S.-Y. Jiang, and S. Fu, Numerical investigation of separation-induced transition in a low-pressure turbine cascade in a low-disturbance environment, Sci. China-Phys. Mech. Astron. **63**, 264711 (2020), https://doi.org/10.1007/s11433-019-1475-8

1 Introduction

Over the last two decades, researchers have devoted intensive efforts to increase the efficiency of blades in LPT to meet the requirements of modern industry. One can achieve this goal by imposing a higher aerodynamic load upon blades, and thus blades are designed with a larger turning angle. In return, an adverse pressure gradient on a blade surface is enlarged, bringing about a detachment of boundary layers from walls. Also, Reynolds number in LPT is so low especially during the high altitude cruise condition that flow at the leading edge of blades is laminar, followed by a transition inside unsteady separation bubbles. The location where transition starts and the spatial extent within which transition takes place influences the LPT performance and is of crucial interest in performance prediction applications [1]. Thus, a good understanding and a reliable prediction of the separation-induced transition are important for LPT aerothermal design.

Unfortunately, since the flow is very three-dimensional and highly complicated, with the occurrence of vortex packets and localized breakdown [2], it is difficult to figure out the instability process in a separation-induced transition. Until now, researchers are yet to reach agreements on the

*Corresponding author (email: fs-dem@tsinghua.edu.cn)

mechanisms that may cause three-dimensionality, let alone accurately modeling the separation-induced transition flow field in LPT. The highly unsteady essence makes the investigations of the flow a big challenge for both experiments and numerical simulations. The early research approaches of the separation-induced transition were mainly experimental study and numerical simulation of two-dimensional flow. It was until the early twenty-first century that high-resolved measures began to be used to predict the separation-induced transition, facilitating investigations of the instability mechanisms.

Based on discussions by previous researchers, in a low-disturbance environment, the instability process starts in the upstream attached boundary layer, in which initial fluctuations have been amplified [3-12] and enter the separated shear layer directly. The K-H instability supposedly thought to be dominant in the flow field with an inflection point in the velocity profile [10] has long drawn the attention of researchers. The primary instability of the separation-induced transition is the convective amplification of two-dimensional waves via the K-H instability mechanism [4,13]. Several researchers have made efforts to verify the dominant role of K-H instability in the separated shear layer. The authors [4,6,14-19] illustrate that the dominant frequency in the primary instability stage falls in the typical frequency range in the free shear layer flows. Dynamic mode decomposition was also used to capture the feature of K-H instability [20]. There is a noticeable difference between the primary instability in the separated shear layer and that in the free shear layer. The viscous effect of the wall somehow affects the former. Several studies have recognized the importance of interaction between T-S (Tollmien-Schlichting) and K-H modes [7,8,12,15-17]. Boutilier and Yarusevych [21] compared the results of viscous and inviscid linear stability analyses, concluding that viscosity does not have a strong effect on the inviscid instability of this flow. An in-depth investigation by Marxen et al. [11] highlighted the evolution of Fourier modes. They suggested that the T-S instability was important only when the bubble was tiny or when the boundary-layer Reynolds number upstream of the bubble was already sufficiently large.

When the diminishing growth of K-H waves occurs, the shear layer rolls up and collapses into individual vortex packets [22]. These individual large scale vortices are called K-H rolls [23], which are initially two-dimensional spanwise ones [24]. The K-H instability drives the formation of these K-H rolls, as emphasized by many investigations [15,25,26]. The three-dimensionality of the flow field occurs closely related to the instability for the K-H rolls. This three-dimensionality always sets in so rapidly that it is hard to recognize the instability mechanisms in terms of a primary, secondary, let alone tertiary instability [27]. Notwithstanding the massive researches on the instability mechanisms in the mixing layer, attentions paid on the instability that causes a three-dimensionality in the separation-induced transition are still limited [28].

Gaster [29] introduced the widely accepted instability mechanisms and absolute secondary instability. These mechanisms were also studied by many following researchers using linear stability theory (LST) or DNS [5,30-32]. Alam and Sandham [30] investigated the absolute or convective nature of the instability of profiles and suggested that the absolute instability happened when the reverse flow magnitude was 15%-20% of the local freestream velocity. An in-depth study by Embacher and Fasel [31] involved non-linear and non-parallel effects based on spatially periodic base flow. They pointed out the relevant role of absolute instability, with the reverse flow being up to 23%. Inspired by the early investigations of bluff-body wakes [33,34], Jones et al. [35] associated a self-sustaining instability with the mode A discussed in refs. [33,34]. This instability is the elliptical instability [36], which causes a spanwise-periodic deformation of the vortex core. Marxen et al. [24] found the ratio of the spanwise wavelength to the primary streamwise wavelength of the fundamental frequency to be 0.451 and of subharmonic instability to be 0.9. Besides, the mode B in the aforementioned studies corresponds to hyperbolic instability in the braid region, where the streamlines are hyperbolic, upstream of each developing vortex. The so-called braids are the streamwise-aligned vortex tubes between consecutive K-H rolls, as reflected in Kurelek et al.'s [19] experiment. Streamwise-oriented smoke filaments connected subsequent K-H rolls in the braid region. This instability mechanism is responsible for a quick disintegration of a spanwise vortex into small-scale turbulence [24]. The spanwise wavelength is 0.2 of the primary streamwise wavelength for the fundamental instability in the cylinder wakes [33] and 0.225 in a separation bubble [24]. Marxen et al. [24] proved the coexistence of both instability mechanisms in the separation-induced transition. Later, Yang and Abdalla [28] made an important discovery by investigating the separation-induced transition without any particular forcing. In their results, the only secondary instability at work was the elliptical instability at the fundamental frequency, even if the streamwise rib vortices were visible in the braid region. They attributed streamwise ribs to the further stretching and titling effect of the K-H roll, which was initially deformed because of elliptical instability. They also pointed out that the three-dimensionality process was sensitive to variations in forcing.

Another potential candidate mechanism for the three-dimensionality process is global instability, which requires a smaller amount of reverse flow magnitude [37]. The self-sustained global instability exists even for flows that are locally absolutely stable downstream of the minimum distance for a feedback mechanism [31]. In contrast to global instability, potential candidate mechanisms can be highly

localized. Görtler type instability [38,39] can arise locally in separating shear flows even in the absence of curved walls, because a weak concave streamline curvature occurs around the separation point [40]. Maskayek and Peltier [41] found a highly localized secondary stagnation-point instability in the mixing layer, capable of ejecting energy into small-scales.

Despite the progress made by recent investigations, researchers still debate whether the secondary instabilities are elliptical or hyperbolic simultaneously in action [28] and whether the braid instability is of hyperbolic nature [3]. The present work attempts to illustrate the elliptical and/or hyperbolic essence of the secondary instabilities in the separation-induced transition in a low-disturbance (<0.1%) environment. DNS of the flow field in the Pak-B blade cascade is performed based on the experiments provided by Huang [42] on one specific condition. We carefully analyze the results in both physical space and Fourier space.

2 Numerical method

2.1 Problem definition

The current case is based on the experiment of a linear cascade consisting of LPT blades Pak-B by Huang [42]. The experiment was under the condition of a broad range of Reynolds numbers and three FSTIs (freestream turbulent intensity). At the lowest FSTI, the separation bubble on the suction side does not reattach under low Reynolds numbers. For higher Reynolds numbers, the length of the reattached separation bubbles decreases as the Reynolds numbers increases. It also decreases as the FSTI increases [42]. The condition with the Reynolds number $Re_\infty=U_\infty C_{ax}/\nu=5\times10^4$ in a low-disturbance environment is chosen to conduct the DNS. The inlet freestream velocity U_∞ is 4.472 m/s, and the axial chord length C_{ax} is 0.1598 m defined in Figure 1. Under this condition, shedding separation vortices in the aft section of the blade are observed on the suction side. This is because the blade spans a 95-deg turn, leading to a large adverse pressure gradient in the channel. The quasi-laminar boundary layer detaches at a fixed location of $x\approx70\%$-$75\%C_{ax}$ (as stated in the experiment, the accurate location is hard to define). A series of vortices shed from the suction surface, and transition happens in the shedding vortices during the downstream convection process towards the trailing edge, as reflected in Figure 2. The time-averaged flow field shows that the boundary layer reattaches at a location of $x\approx97.5\%C_{ax}$, forming an enclosed average separation bubble. The flow field under this condition is a typical laminar separation/short bubble mode, as classified by Hatman and Wang [7]. The purpose of this paper is to clarify the instability mechanisms of this separation-induced transition mode.

The x-coordinate axis is in the axial direction of the cascade, and the origin of the coordinate system is set at the location which possesses the minimum x-coordinate value along the blade.

2.2 Numerical methods for DNS

A brief description of the mathematical formulation is given in this subsection, and the details are described in Jiang and Fu's paper [43]. We use an in-house code for DNS based on a

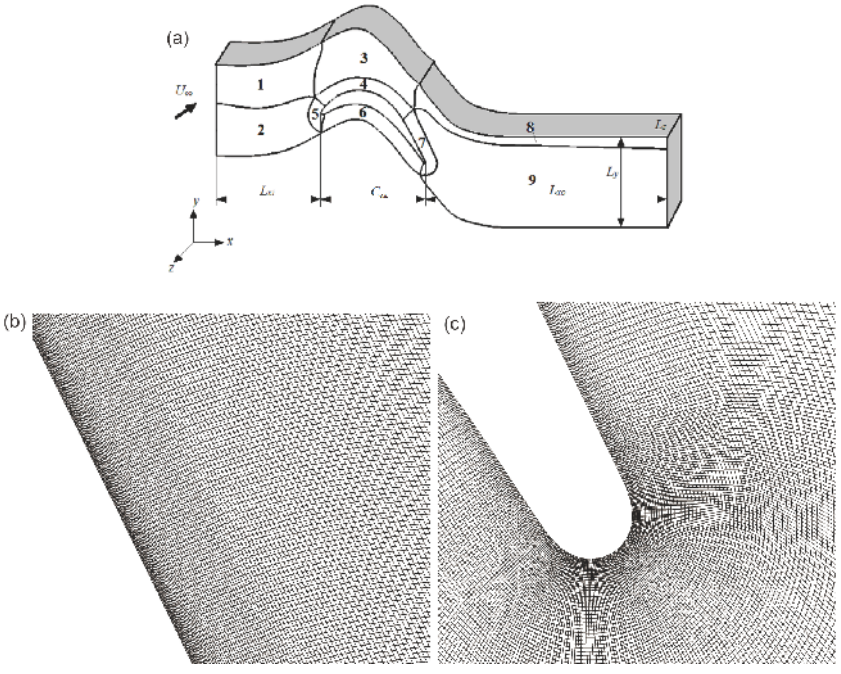

Figure 1 Computation domain and the grid of G_{DNS}. (a) Entire block structure; (b) separation region; (c) trailing edge.

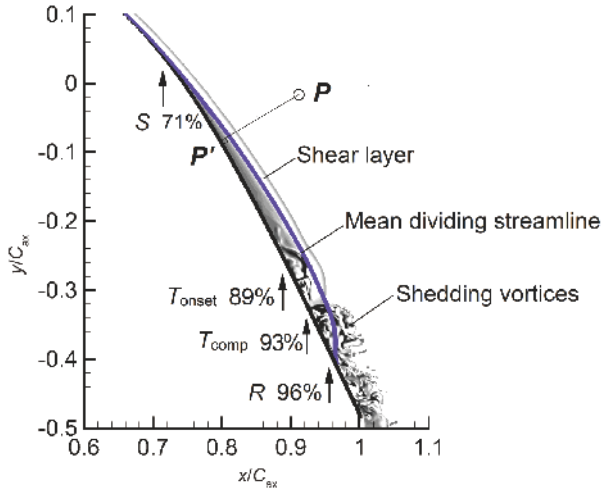

Figure 2 (Color online) Sketch for the separation region.

modified semi-implicit method for pressure linked equation (SIMPLE) algorithm. An modified momentum interpolation method (MMIM) [44] is used to instead of Rhie and Chow's method [45]. Considering that in DNS, the time scale is on the dissipative scale, this small time step can lead to unphysical oscillation if Rhie and Chow's method is used [46]. An implicit scheme of third-order time accuracy is adopted. Minimized dispersion and controllable dissipation (MDCD) reconstruction by Wang et al. [47] is employed for the convective terms in momentum equations to minimize the numerical error and optimize spectral property. This numerical algorithm is suitable for DNS and can capture rich flow structures on affordable computational grid points.

Figure 1(a) exhibits the computational domain for DNS. The inlet boundary is $L_{xi}=C_{ax}$ upstream of the leading edge, and the outlet boundary is $L_{xo}=2C_{ax}$ downstream of the trailing edge. According to the experiment, the pitchwise extent is $L_y=0.1412$ m. The spanwise extent L_z is set to be $0.2C_{ax}$, which was proved to be adequate by Rizzetta and Visbal [48].

According to the experimental data, FSTI is controlled to be about 0.08% around the leading edge, and white noise is added to the inlet boundary to generate this very low FSTI environment following the approach for a similar situation by Yang and Abdalla [28]. We also tested the case upon the removal of any inlet fluctuations. Nevertheless, the various inlet conditions result in little difference in the mean flow field, as well as power spectral density (PSD) at the vortex formation and breakup stage. The only visible difference exists around the separation point and the upstream boundary layer, where some peaks in spectra possessing smaller energy in the no-inlet-fluctuation case. This difference generally disappears in the aft portion of the primary instability stage. This transition process seems to be self-sustained because turbulent flow structures remain upon removal of any inlet fluctuations. In pitchwise and spanwise direction, a periodic boundary condition is employed. The second-order accurate interpolation is adopted for the outlet boundary. At $x>2.5C_{ax}$, the grid size is enlarged to set up a buffer zone to avoid unphysical reflections from the outlet boundary. The results show that the unphysical reflection from the boundary is constrained within three layers of grids.

The grid used for DNS is labeled with "G_{DNS}", with its details shown in Figure 1(b) and (c). Its grid density in the x-y plane is displayed in Table 1. 180 grid points are distributed uniformly in the spanwise direction. As seen in Table 1 and Figure 1(b), refinement of the grid is conducted in the aft section of the blade on the suction side, where the separation-induced transition happens. The amount of the grid points is 75 million. The grid is periodic in pitchwise and spanwise directions.

A check of the grid resolution is done by comparing it with the other DNS studies of the separation-induced transition, as is presented in Table 2. The maximum value of the skin friction coefficient $C_{f\,max}$ of 0.01 is used for evaluating the resolution. The first wall-normal grid space is $\Delta y^+_{max}=0.68$ in wall units. Following the manner by Alam and Sandham [30], the resolution is compared by tabulating the number of points for $y^+<9$ shown in Table 2. In the streamwise and spanwise directions, the grid resolutions are $\Delta x^+_{max}=4.42$ and $\Delta z^+_{max}=3.94$. The resolution used in the present study is comparable to that of the other DNS cases using spectral method [24,30] and finite difference [35] in spanwise direction.

Moreover, grid-independence is checked with the other two grids, labeled with "G_{Coarse}" and "G_{Fine}", whose grid

Table 1 Grid density distribution

block	G_{DNS}	G_{Coarse}	G_{Fine}
1	120×80	96×64	120×80
2	120×82	96×64	120×100
3	323×80	256×64	453×80
4	323×160	256×128	453×198
5	82×160	64×128	100×198
6	323×160	256×128	453×198
7	533×160	352×128	652×198
8	280×80	204×64	320×80
9	533×280	352×224	652×320

Table 2 Grid resolution in wall units

Case	Δx^+	Δy^+ at $y^+=9$	Δz^+	N ($y^+<9$)
G_{DNS}	4.42	0.90	3.94	12
Marxen et al. [a)]	3.00	0.83	3.17	12
Alam and Sandham [b)]	20.73	0.90	6.20	16
Jones et al. [c)]	3.36	>1.0	6.49	<10

a) See ref. [24], b) see ref. [30], c) see ref. [35]

densities in the *x*-*y* plane are listed in Table 1. The grid densities in *z* direction are the same as grid G_{DNS}. The main difference is in the separation region, where the grid size of G_{Coarse} is about 0.75 of G_{DNS} and the number of the grids is nearly half. One-dimensional variables on different grids, namely wall-pressure coefficient and skin friction coefficient, are compared in Figure 3, as well as the velocity profiles normalized by $U_{\mathrm{mid\text{-}channel}}$ (the local streamwise freestream velocity in the blade passage) in Figure 4, which are discussed in sect. 3.1.

The initial condition for the DNS is obtained from the RANS (Reynolds-averaged Navier-Stokes) result computed on the DNS grid. With this initial flow field, 2×10^4 time steps are calculated to obtain a convergent solution, and 1.2×10^5 more time steps within more than 300 vortex shedding periods are used for the long-term values of the turbulence statistics. With these time steps, a statistically steady state is reached. The time step size is 1×10^{-5} s, small enough to capture the turbulent structures.

2.3 Numerical methods for URANS

Two-dimensional unsteady Reynolds averaged Navier-Stokes (URANS) equations are solved with the $Re_{\theta\text{-}\gamma}$ model [49] for comparison. The convective terms in the URANS equations are discretized with the second-order upwind scheme. The diffusive terms are approximated by the central scheme. The grid is two-dimensional, and the computational domain is the same as that for DNS in the *x*-*y* plane, with 5×10^4 grid points employed. Attempts were also made with the transition models developed by Wang et al. [50,51], but these models did not predict the flow field well under the current situation.

2.4 Post-processing

In DNS result, 8×10^4 data collected during more than 200 periods of fundamental instability have been used for Fourier transform in time to investigate the evolution of the fluctuations. The Fourier transform is based on the streamwise fluctuation velocity on the monitor points with a step of Δt. *f* represents the frequency in time, and power spectral density (PSD) is used to demonstrate the energy on different frequencies. Welch's method with a Hanning window function is applied. The signal is split up into 100 overlapping segments (the overlapping length is 400) of length 4×10^4.

Double Fourier transform during 80 periods of the fundamental frequency is taken in *t* and *z* directions. (*h*, *k*) is used to specify Fourier modes. *h* and *k* represent the normalized wavenumber in time and spanwise, respectively. The fundamental frequency for normalization is f_{v}=265 Hz, which is discussed in the next section. The spanwise wavenumber *k*=1 corresponds to the wavelength of $0.2C_{\mathrm{ax}}$. Mode amplitude is defined as $|\hat{u}'|$. The time step used for Fourier analysis is $5\Delta t$. An inverse double Fourier transform is used to restore the physical flow field associated with a specific mode (*h*, *k*).

Phase- and spanwise-average based on fundamental frequency is performed also during 80 fundamental periods. In the results, a series of vortex sheds from $84\%C_{\mathrm{ax}}$. The streamlines are hyperbolic between the consecutive vortices and elliptical in the vortex core. We trace the saddle point of the hyperbolic streamlines and the vortex core in a phase and obtain the phase- and spanwise-averaged saddle point trajectory and vortex core trajectory, respectively.

Several derived quantities are computed. These key parameters are described in this subsection. The wall-pressure coefficient is

$$C_p = \frac{\langle p_{\mathrm{w}} \rangle - p_\infty}{0.5\rho U_\infty^2}, \tag{1}$$

where $\langle p_{\mathrm{w}} \rangle$ is the average wall-pressure and p_∞ is the inlet pressure, ρ is the density of the gas, which is set to a constant in incompressible flows. The skin-friction coefficient is

$$C_f = \frac{\tau_{\mathrm{w}}}{0.5\rho U_\infty^2}, \tag{2}$$

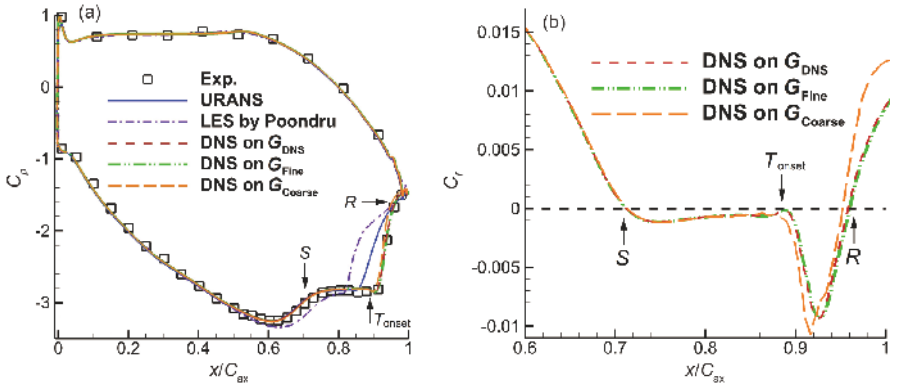

Figure 3 (Color online) Time-averaged and spanwise-averaged coefficient curves compared with experimental data [42] and LES data by Poondru [52]. (a) Wall-pressure coefficient by different methods (*S*, *R* and *T* mark the time-averaged separation point, reattachment point and transition onset in the result on G_{DNS}, respectively). (b) Skin-friction coefficient by DNS.

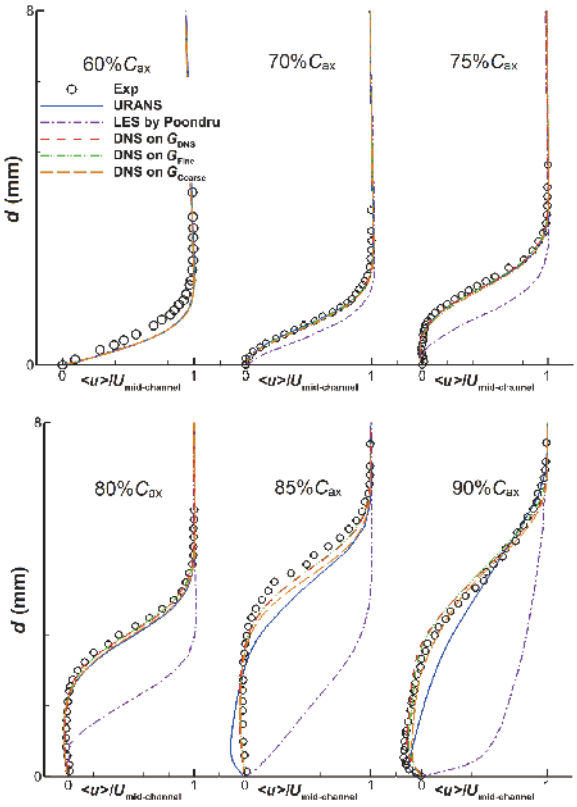

Figure 4 (Color online) Time-averaged and spanwise-averaged streamwise velocity profiles at different stations compared with experimental data [42]. d is the wall-normal distance.

where the wall shear stress τ_w is defined as:

$$\tau_w = \mu \frac{\partial \langle u \rangle}{\partial n}. \tag{3}$$

In eq. (3), n stands for the wall-normal coordinate, and μ is the viscous coefficient. $\langle u \rangle$ is the average streamwise velocity paralleling to the wall. This case is a planar cascade. Thus not only time-average but also spanwise-average is calculated for DNS. For the two-dimensional URANS, the flow field is only averaged in time. The fluctuation variables are obtained by

$$\varphi' = \varphi - \langle \varphi \rangle, \tag{4}$$

where φ stands for any instantaneous variable, such as velocity and pressure, $\langle \varphi \rangle$ is the average value. Reynolds stresses are calculated with these fluctuation variables respectively. A noteworthy variable is the TKE, which is determined as:

$$\text{TKE} = \frac{1}{2}\left(\langle u'u' \rangle + \langle v'v' \rangle + \langle w'w' \rangle\right). \tag{5}$$

Although in the strict sense, TKE should not be recognized as fluctuation kinetic energy before the transition, we still use the term "TKE" for laminar fluctuations without distinguishing for simplicity in the following discussions. The three Reynolds stresses in eq. (5) are in the streamwise, wall-normal and spanwise directions, respectively, instead of the directions of coordinate axes of the Cartesian coordinate system.

The displacement thickness δ_1 and momentum thickness δ_2 are determined using the average streamwise velocity profiles as:

$$\begin{aligned} \delta_1 &= \int_0^{d_{\text{mid-channel}}} \left(1 - \frac{\langle u \rangle}{U_{\text{mid-channel}}}\right) \mathrm{d}n, \\ \delta_2 &= \int_0^{d_{\text{mid-channel}}} \frac{\langle u \rangle}{U_{\text{mid-channel}}} \left(1 - \frac{\langle u \rangle}{U_{\text{mid-channel}}}\right) \mathrm{d}n, \end{aligned} \tag{6}$$

where $d_{\text{mid-channel}}$ is the wall-normal distance, $U_{\text{mid-channel}}$ is the average streamwise velocity gained from the middle of the channel, where the variables hardly change in the wall-normal direction. These integrals are solved numerically.

The shape factor H_{12} is

$$H_{12} = \delta_1 / \delta_2. \tag{7}$$

One thing that should be noticed before the discussion is that we use the streamwise station to describe the location of a point in the flow field. As illustrated in Figure 2, the point P' is the projection of P on the blade surface. The x-coordinate of P' is used to describe the streamwise station.

3 Mean flow

An accurate prediction of this separation-induced transition is of great challenge. In Figure 3(a), Large eddy simulation (LES) by Poondru [52] predicted an early reattachment, as reflected by C_p of the transition region deviating greatly from the experimental data, let alone the velocity profiles. As for URANS, the $Re_{\theta\text{-}\gamma}$ model manifests surprisingly good agreements with the experimental data for C_p, as well as the velocity profiles in the fore portion of the separation region in Figure 4. However, the velocity profiles do not match well with the experiment at station 85%C_{ax} and 90%C_{ax} because of an early reattachment (see Figure 3(a)). This is the consequence of the overrated growth rate of TKE by the $Re_{\theta\text{-}\gamma}$ model during the transition process. Therefore, only DNS gives a reliable prediction of this complicated flow field.

Comparisons of the results on different grids are made, as demonstrated in Figures 3 and 4. In Figure 3(a), a slight deviation is observed in the result by G_{Coarse}, which seems ignorable. However, the deviation is severer, as reflected in Figures 3(b) and 4, indicating an early reattachment. In Figure 3(b), the skin friction coefficient by G_{Coarse} is inconsistent with the other two at x>85%C_{ax} and likewise, corresponding difference is observed in the last two velocity profiles in Figure 4, which reveals that the coarse grid size is not small enough for directly predicting the transition process and turbulent boundary layer.

The result by G_{DNS} is much more reliable. In Figure 3(a), the wall-pressure coefficient curves by G_{DNS} and G_{Fine} are

identically in good agreement with the experiment, as well as the velocity profiles in Figure 4. A good match of the velocity profiles, even for the small negative velocity in the near-wall region, suggests that the results were grid-independent at this level of grid size. Nevertheless, a slight difference is observed at x>85%C_{ax} with the experimental results, revealing the effect of the numerical error. Fortunately, this difference is so small that it will not affect the authenticity of the result by G_{DNS}. The resolution of G_{DNS} is adequate, and overall the result is physical. Therefore, it is chosen for further discussions.

The average separation, reattachment, and transition points are obtained according to the information reflected by C_f presented in Figure 3(b). A sharp decrease of C_f is found before separation due to the deceleration of flow in the channel. The average separation point is at 71%C_{ax}, where C_f changes from positive to negative. Around x=88%C_{ax}, a small overshoot of C_f arises, which is closely followed by a sharp growth of the absolute value of the skin-friction coefficient. The start point of this sharp growth corresponds to the transition onset. This location just slightly precedes the maximum mean displacement thickness location of 90%C_{ax}, as shown in Figure 5, where the displacement thickness δ_1 reaches its maximum. This phenomenon is coincidental with Hatman and Wang's [7] observation for laminar separation/short bubble mode. At x=90.5%C_{ax}, the wall-pressure coefficient C_p reaches its minimum, shown in Figure 3(a). The maximum negative C_f is at x=93%C_{ax}, where is the maximum reverse-flow intensity position. The computed separation bubble reattaches at x=96%C_{ax}.

Figure 5 shows the displacement thickness δ_1, momentum thickness δ_2, and shape factor H_{12}. The shape factor H_{12} starts with a value of H_{12}=2.6, the typical value of the attached laminar boundary layer. A slight decrease of the shape factor is observed, to the minimum value of 2.51. The rapid increase of δ_1 begins approximately from the separation point, leading to an increase of H_{12}. Then a local minimum value of H_{12} is observed, as δ_2 reaches its local maximum. In the discussions above, this location is where a small overshot of the skin friction coefficient is found in Figure 3(b). Then the momentum thickness δ_2 experiences rapid growth as the transition happens. Towards the average reattachment point, the growth of δ_2 slows down and δ_1 keeps decreasing. After the reattachment point of 96%C_{ax}, the growth rate of δ_2 is extremely low, preventing H_{12} from rapidly decreasing. Then H_{12} slowly goes down to its minimum value of 1.75 at the trailing edge.

4 Fluctuation statistics

In this section, the fluctuation statistics are discussed to help explain the secondary mechanisms of the separation-induced

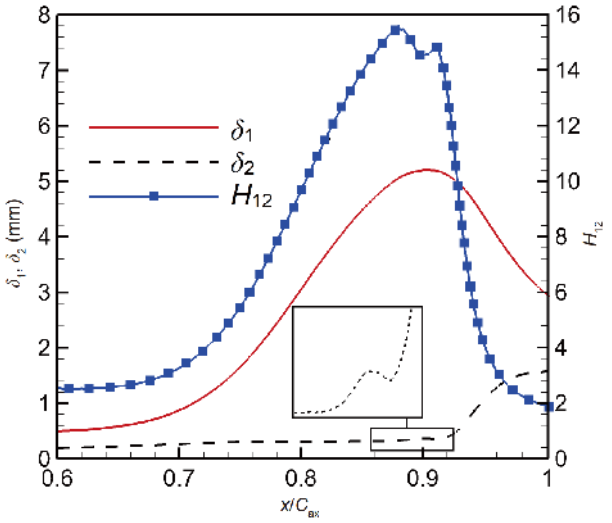

Figure 5 (Color online) Displacement boundary layer thickness δ_1, momentum boundary layer thickness δ_2 and shape factor H_{12}.

transition. Before focusing on the transition process, we first have an overall image of the flow field and create a general frame of this flow field. Figure 6(a) shows the overall TKE contour as well as the average streamline and the line of maximum TKE. With the information from this figure and sketch for the separation region in Figure 2, we can divide the instability process into three stages: primary instability, secondary (or even ternary) instability in the vortex formation region and the vortex breakup region.

Primary instability refers to the dominant growth of TKE and streamwise fluctuation velocity u' in the separated shear layer upstream of the vortex formation region, as reflected by Figure 6(a) and (b). TKE is amplified, reaching a maximum at 93%C_{ax} in the vortex breakup region downstream of the average vortex core. After reattachment, TKE maintains at a high level during the relaxation process of the turbulent boundary layer, and gradually decays in the wake.

4.1 Fluctuation statistics in the shear layer before the vortex formation

In Figure 6(a), TKE dominantly grows in the shear layer, suggested by the superposition of the maximum spanwise vorticity line and maximum TKE line. In Figure 7, the spanwise and wall-normal fluctuations are more than two orders of magnitude smaller than those in the streamwise direction in the upstream boundary layer, which are further suppressed in the separated shear layer at the primary instability stage. Figure 8 reveals the PSD at the points in the shear layer. Comparing the spectra at station 70%C_{ax} in the attached laminar boundary layer and station 75%C_{ax} in the separated shear layer at the primary instability stage, we can observe the similar energy distributions. It is logical to consider primary instability in the separated shear layer to be

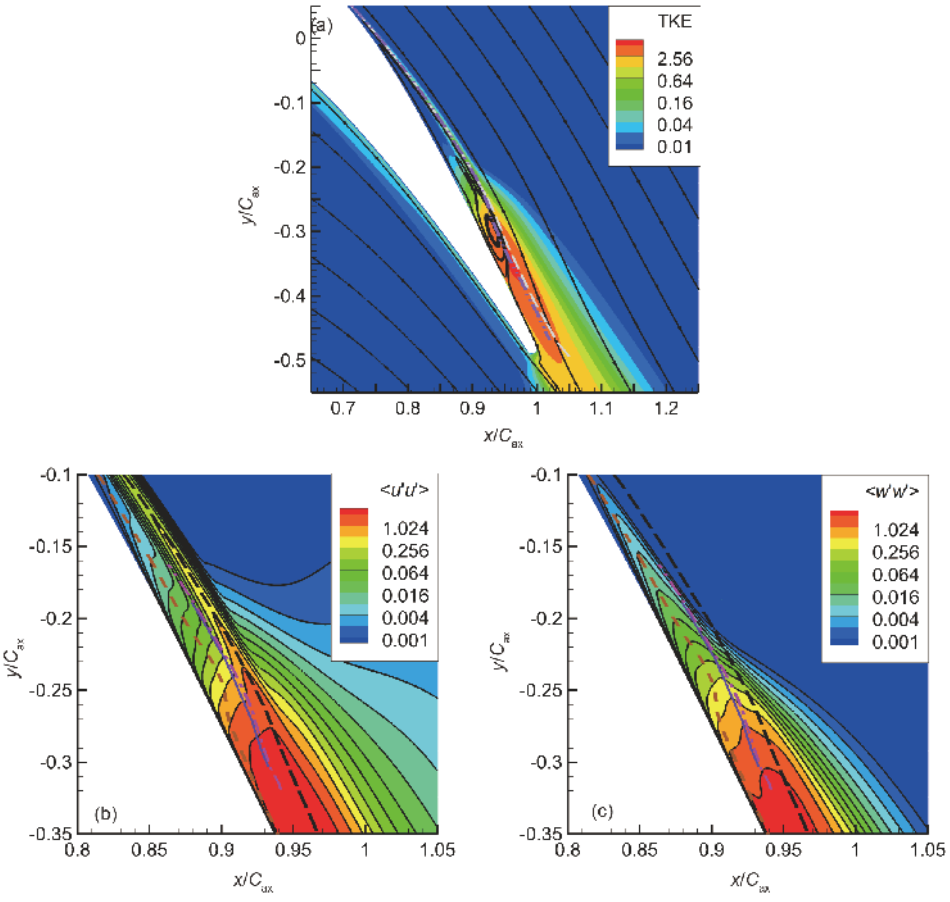

Figure 6 (Color online) Contours of fluctuation statistics. (a) Overall TKE with average streamlines, (b) $\langle u'u' \rangle$, (c) $\langle w'w' \rangle$. Long dashed line: maximum spanwise vorticity; short dashed line: maximum reverse velocity line; dash-dot line: maximum TKE; solid line: phase- and spanwise-averaged saddle point trajectory.

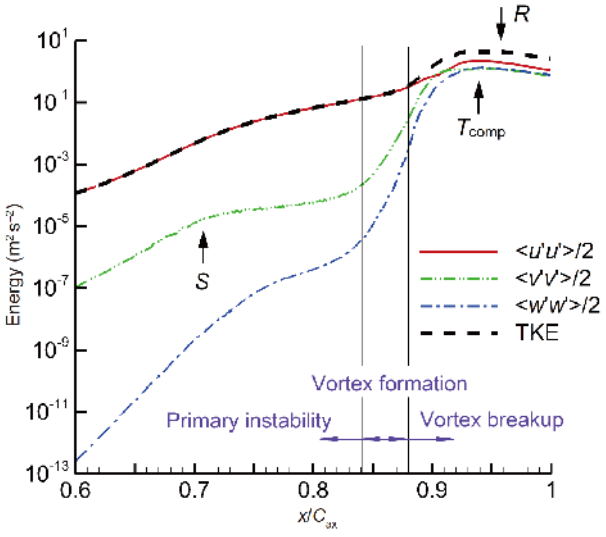

Figure 7 (Color online) Evolution of TKE in the near-wall regions and its maximum value.

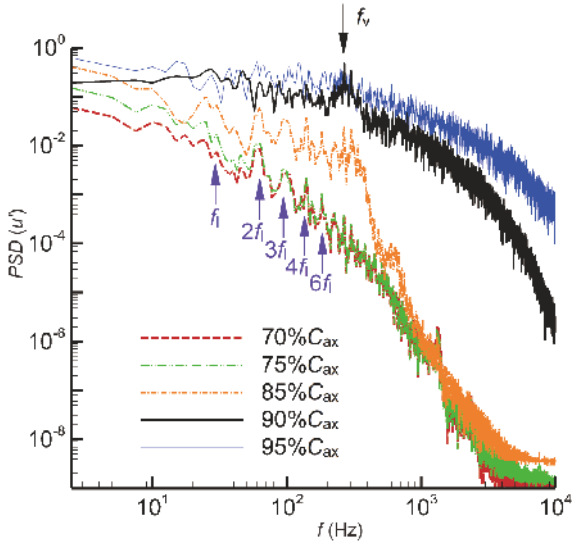

Figure 8 (Color online) PSD of streamwise fluctuation velocity in t direction, monitor points along the maximum spanwise vorticity line.

an extension of the instability process of the attached boundary layer. The energy of high frequencies does not increase in the fore portion of the shear layer, while that of the frequencies lower than 100 Hz experiences a mild increase.

The distinct peaks in the shear layer (see lines labeled as "70%C_{ax}" and "75%C_{ax}" in Figure 8) are actually in connection with f_v=265 Hz which corresponds to the shedding

frequency of two-dimensional K-H rolls. The vortex shedding frequency is calculated from the shedding period T_v ≈0.0037 s estimated as the time interval of consecutive K-H rolls. We mark the peak of $1/8f_v$ as f_l in the figure. The other peaks, including the peak f_v, are the harmonics of f_l. The energy of the 265 Hz waves starts to increase sharply in the fore portion of the primary instability stage. For separated shear layer, the typical Strouhal number $Sr_{\delta 2s}=f_v\delta_{2s}/U_{es}$ for the K-H instability, based on the shedding frequency f_v, momentum thickness δ_{2s} and boundary-layer-edge velocity U_{es} at the separation point, has been reported in many literatures, including 0.005-0.01 by Yang and Voke [18] and 0.008-0.013 by McAuliffe and Yaras [17]. In the current case, Strouhal number $Sr_{\delta 2s}$ is 0.0093, falling in the typical range for K-H instability. This is the evidence that the dominant instability mechanism at the primary instability stage is inviscid K-H instability.

4.2 Fluctuation statistics in the vortex formation and vortex breakup region

The vortex formation region starts at about 84%C_{ax}, where the separated shear layer rolls up into a quasi-two-dimensional vortex, namely K-H roll. In Figure 7, although the streamwise fluctuation is still dominant in the shear layer, the difference arises when the K-H roll forms. Both wall-normal Reynolds stress $\langle v'v' \rangle$ and spanwise Reynolds stress $\langle w'w' \rangle$ experience the dramatic growth in the vortex formation and breakup region until they reach the same order of magnitude as $\langle u'u' \rangle$. As a result, TKE also receives a boost, where the transition is considered to happen. It is not a surprise that $\langle v'v' \rangle$ surges in the vortex formation region since the vortex intensifies the wall-normal flow. Nevertheless, the growth of $\langle w'w' \rangle$, which indicates the appearance of three-dimensional flow structures, is not necessary.

In the vortex formation region (see the line labeled as "85%C_{ax}" in Figure 8), the energy growth concentrates mainly on the band of [30 Hz, 300 Hz], which is much wider than that at primary instability stage. In the vortex breakup region (see the line labeled as "90%C_{ax}" and "95%C_{ax}"), the unstable band broadens across an even wider range of frequencies, especially the high frequencies. The shedding frequency f_v=265 Hz becomes the most energetic frequency at 90%C_{ax}. However, in the aft portion of the vortex breakup process, the peak of 265 Hz disappears as a result of the relaxation process of the reattached boundary layer.

The evolutions of oblique modes (h, k) in Figures 9 and 10 are used to clarify the mechanisms responsible for three-dimensionality. Three typical frequencies of the modes, namely fundamental frequency f_v and its subharmonics $f_v/2$, $f_v/4$ (corresponding to h=1, 0.5, 0.25), are investigated. We also check all the spanwise wavenumbers k between 0 and 14. Only the modes possessing particular features are exhibited in the figures, while the others are just briefly described in the text.

In Figure 9(a) and (b), the two-dimensional modes (1, 0), (0.5, 0) and (0.25, 0) possess much larger amplitudes if compared with their respective oblique modes, especially the mode (1, 0). The mode (0.25, 0) starts to increase at 78%C_{ax} after a sluggish growth, while the mode (0.5, 0) increases quickly from 76%C_{ax}. The mode (1, 0) gains the largest growth rate in the aft portion of the primary instability process from 80%C_{ax} after a short negative growth. It quickly becomes the most-amplified mode in the vortex formation region. The situation is different from the forced separation-induced transition by Marxen et al. [24]. In their case, the mode (1, 0) was excited upstream of the bubble and possessed the largest amplitude in the whole flow field, while modes (0.5, 0) and (0.25, 0) were less energetic (see Figure 12(a) in ref. [24]). The same situation was observed for the subharmonic oblique modes (see Figure 11 in ref. [24]). In the current case, in the fore portion of the vortex formation

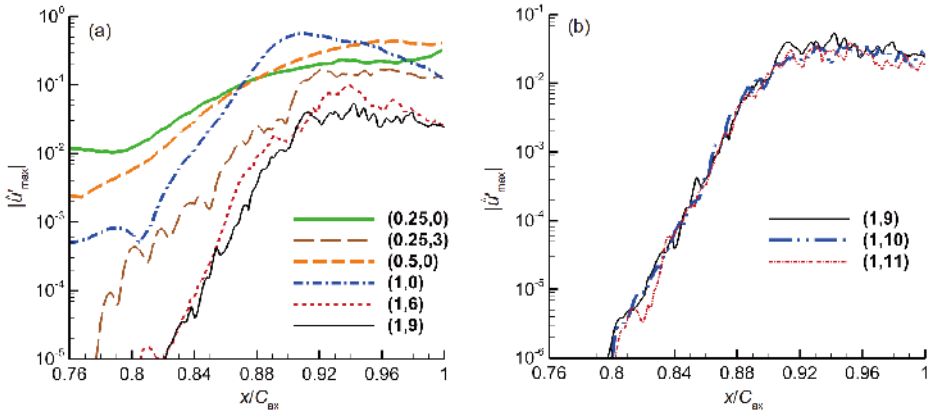

Figure 9 (Color online) Amplification curves for the maximum streamwise fluctuation $|\hat{u}'_{max}|$. (a) Comparison among different modes; (b) fundamental oblique modes with high wavenumbers.

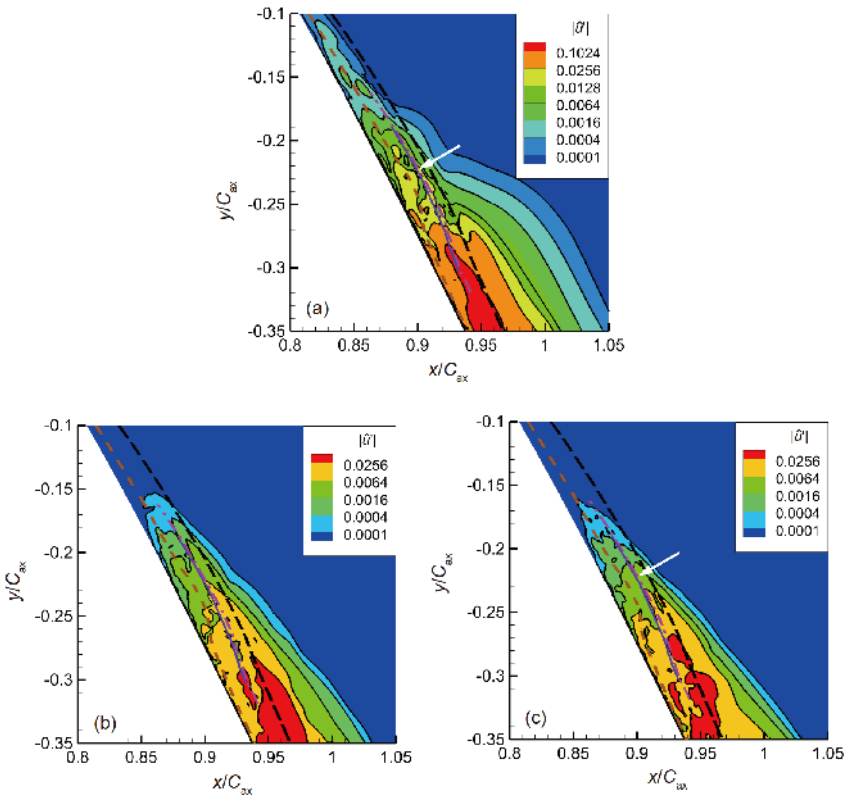

Figure 10 (Color online) Contours of streamwise fluctuation velocity amplitudes $|\hat{u}'|$ for different modes (h, k). (a) (0.25, 3); (b) (1, 6); (c) (1, 9). Long dashed line: maximum spanwise vorticity; short dashed line: maximum reverse velocity; solid line: phase- and spanwise-averaged saddle point trajectory; dash-dot line: phase- and spanwise-averaged vortex core trajectory.

region, the dominate modes are still in low-frequency range (see Figure 8 and Figure 9(a)), with the modes (0.25, k) being nearly one order of magnitude larger than the modes (1, k) at 84%C_{ax}. These gaps have been narrowed downstream since the modes (1, k) have a greater growth rate. Apart from the fundamental modes with high wavenumbers, which stop increasing at 91%C_{ax}, the other oblique modes saturate at about 93%C_{ax}.

In Figure 10, before K-H roll forms, all the oblique modes are active only in the dead-air region along the line of maximum reverse velocity. The phenomenon may be attributed to the three-dimensional structures travel slowly upward with near-wall reverse flow. Turning back to the contour of $\langle w'w' \rangle$ in the vortex formation region in Figure 6(c), we can also find out that $\langle w'w' \rangle$ keeps its maximum along the maximum reverse velocity line in the dead-air region and the fore portion of the vortex formation region. It then turns towards the phase-averaged saddle point trajectory. For $\langle u'u' \rangle$ in Figure 6(a), we can also find its preferential growth near the saddle point trajectory, leading to a weak local maximum on the trajectory line from station 88% C_{ax} to 91%C_{ax}. These varieties may suggest that hyperbolic instability promotes the three-dimensionality of the flow field strongly. However, the trajectory of the phase-averaged saddle point is close to the trajectory of the vortex core, making it not easy to distinguish the hyperbolic instability mechanism from the elliptical instability mechanism. It is necessary to give a further analysis based on the double Fourier transform. The following paragraph concentrates on the amplitudes of Fourier modes and the instantaneous streamwise fluctuation velocity for a specific mode via inverse double Fourier transform. The former is useful in picking out the unstable modes near the average trajectories, and the latter is helpful to distinguish the elliptical instability from the hyperbolic instability.

The shapes of streamwise amplitude in the vortex formation region for oblique modes with h=0.25 are exhibited in Figure 11(a). The period for these modes is 4 times the fundamental period. For k=3-4, a new local maximum of $|\hat{u}'|$ emerges near the phase-averaged saddle point and vortex core position. The primary streamwise wavelength is estimated to be λ_{x0}=0.0998C_{ax} obtained from the instantaneous streamwise fluctuation velocity contour for mode (1, 0). Thus the ratio between the spanwise wavelength λ_z and fundamental streamwise wavelength λ_{x0} falls in the range of 0.501-0.668. The contour of $|\hat{u}'|$ for mode (0.25, 3) is shown in Figure 10(a) as a representative, and the other mode

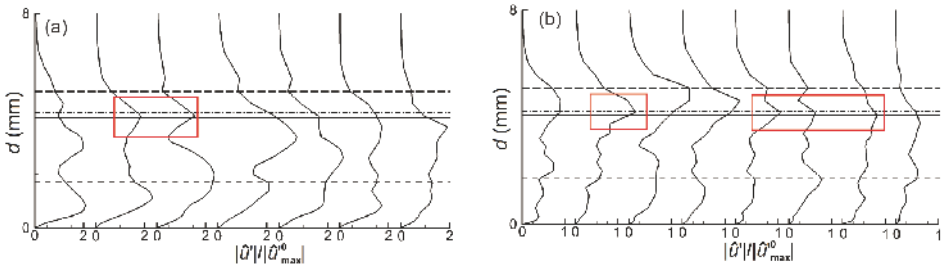

Figure 11 (Color online) Streamwise fluctuation velocity amplitudes $|\hat{u}'|$ for different modes (h, k), normalized by $|\hat{u}'^{0}_{\max}|=|\hat{u}'^{(1,9)}_{\max}|$ station x=88%C_{ax} in (a). (a) h=0.25, k=2, 3, 4, 5, 6, 7, 8 (from left to right); (b) h=1, k=5, 6, 7, 8, 9, 10, 11, 12 (from left to right). Thin line: the location of phase- and spanwise-averaged vortex core; thick line: the location of phase- and spanwise-averaged saddle point.

evolves similarly. A new peak arises in the aft portion of the vortex formation region and exists between station 87%C_{ax} and 90%C_{ax}. Figure 12 reveals the instability mechanism related to the peak. In Figure 12(a), we can see a thin strip of positive u' between station 87%C_{ax} and station 90%C_{ax}. The intensity of the strip is enhanced as the saddle point of the instantaneous streamlines passes, as shown in Figure 12(b). This is followed by its dissipation as the saddle point leaves in Figure 12(c) and (d). This mode is not sensitive to elliptical instability, as shown in Figure 12(c) that it continues to vanish in the vortex core. This strip does not convect with the K-H rolls and vanishes to zero in the next fundamental period. During the third fundamental period, it is negatively enhanced in the braid region similar to the first fundamental period. Therefore, with the help of instantaneous amplitudes, evidence is provided for hyperbolic instability for low-frequency waves.

In Figure 11(b), for fundamental modes with h=1, two kinds of secondary instability mechanisms can be seen in the vortex formation and breakup region. The modes with k= 9-11 are excited at the location of the average saddle point, as marked with a box in the figure. Figure 10(c) shows the

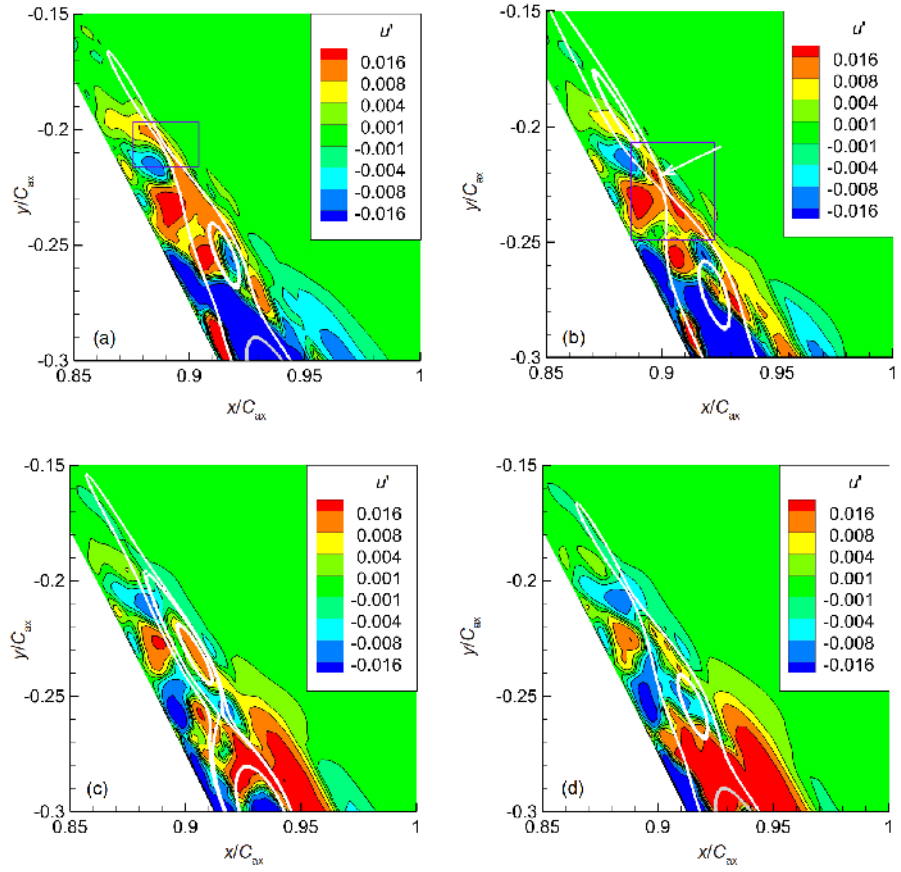

Figure 12 (Color online) Contours of u' amplitudes for mode (0.25, 3) together with instantaneous streamlines computed from modes (0, 0) and (1, 0). (a) t=0; (b) $t=t_0+0.25T_v$; (c) $t=t_0+0.75T_v$; (d) $t=t_0+T_v$. The braid region is marked by the box.

contour of amplitude for mode (1, 9). In this figure, at station 87%C_{ax}, a local maximum in the braid region emerges as soon as the saddle point appears and maintains its value as a maximum, suggesting the relevant role of the hyperbolic instability. In the instantaneous flow field in Figure 13(a), a local maximum for this mode is in the same position. This local maximum convects downstream with saddle point as shown in Figure 13(b)-(d), during which it is intensified. At t=0.75T_v, the streamwise fluctuation velocity in the braid region emphasized by a box in the figures is about one order of magnitude larger than that at t=0. During this process, the shape of the local maximum is elongated in the "stretching" direction (the direction of principal extensional strain) of the hyperbolic base flow by the "stretching" effect [53], which is typical in hyperbolic instability. It gradually merges with the downstream fluctuations in the vortex breakup region. The mode (1, 9) possesses a ratio between the spanwise wavelength λ_z and λ_{x0} of 0.223, which is consistent with the ratio of 0.225 in Marxen et al.'s [24] case and 0.2 for Mode B in ref. [34], associated with the hyperbolic instability by Jones et al. [35]. The spanwise wavelength λ_z of fundamental modes excited in the braid region falls in the range of 0.182-0.223λ_{x0} in the current case. The modes (1, 9-11) evolve in almost the same manner and their amplification curves for $|\hat{u}'_{\max}|$ are almost the same in the vortex formation region, as shown in Figure 9(b).

The other secondary instability mechanism is associated with the mode (1, 6), with the maximum of its amplitude $|\hat{u}'|$ locating in the same position as mode (1, 9) (see Figure 11 (b)). In fact, this maximum emerges at station 88%C_{ax} and disappears at station 90%C_{ax} in Figure 10(b). From the instantaneous streamwise fluctuation velocity contour shown in Figure 14(a) and (b), we can also see the transient excitation of the mode in the vortex core between station 88%C_{ax} and 90%C_{ax}. Comparing with mode (1, 9) in Figure 9(b), we can see the growth rates of these modes are almost the same in this region. The spanwise wavelength λ_z is 0.334λ_{x0}, falling in the range of 0.200-0.400 by Maucher et al. [32] for the fundamental elliptical instability (calculated from Figure 3 in ref. [32]). The good agreement convinces the existence of elliptical instability, although it just comes into effect in a short distance.

The subharmonic modes are also checked, whose contours of $|\hat{u}'|$, however, are less regular, with various local maxima

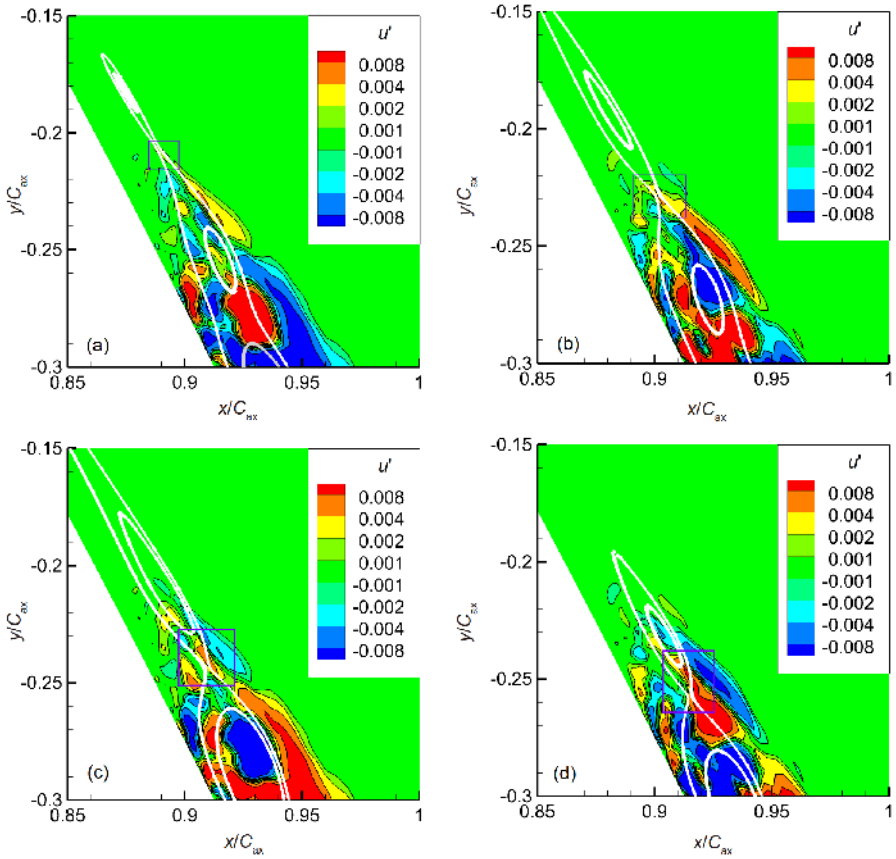

Figure 13 (Color online) Contours of u' amplitudes for mode (1, 9) together with instantaneous streamlines computed from modes (0, 0) and (1, 0). (a) t=0; (b) t=0.25T_v; (c) t=0.5T_v; (d) t=0.75T_v. The braid region is marked by the box.

being visible. The subharmonic modes are always associated with the pairing of K-H rolls [28]. Thus it is likely that no vortex pairing exists. More evidence about this secondary instability mechanism in the physical space is discussed in the next section.

Besides, we supplement two noteworthy things here. Firstly, in Figure 10(b) and (c), before hyperbolic instability or elliptical instability comes into effect, a local maximum is found at the bottom of the shear layer for modes (1, 6) and (1, 9). The other fundamental modes with the spanwise wavenumber k lying within a wide range of 2-12 possess a similar feature. In the shear layer, all the fundamental oblique modes share almost the same phase velocity and streamwise wavelength, as well as the mode (1, 0). Although the unstable wavepackets originate at the very upstream station in the aft portion of the primary instability stage, their fluctuation intensities are weaker than that in the braid region (see Figure 13(a) and (b)) and the vortex core (see Figure 14 (a)) at the transition onset (station 88%C_{ax}). But after the transition, their energy experiences a sharp increase and reaches the same level as that in the braid region (see Figure 13(c) and (d)) or vortex core (see Figure 14(b)). In Figure 13 (a)-(c), the unstable wavepackets are also likely to be affected by the "stretching" effect of the hyperbolic base flow, as they are also elongated in the same direction as the wavepackets in the braid region.

Secondly, Figures 10 and 11 show some other high-energy regions. The most noteworthy feather is that the modes possess large amplitudes in the near-wall region. From Figure 12, we can find that the wavepackets in the near-wall region travel upstream. This is possible due to the feedback effect by global instability that wavepackets from downstream might entrain turbulent fluid, which possibly affected transition [2]. Apart from the two types of instability mechanisms causing three-dimensionality investigated in the current manuscript, the global instability may also be active, since the maximum reverse flow velocity magnitude reaches 19% of the local freestream velocity. The two kinds of mechanisms require an in-depth investigation via stability analysis, which can be the focus of future works.

5 Secondary instability mechanisms and flow structures

As reported in sect. 1, secondary instability mechanisms of the separation-induced transition have not been well understood until now. In this section, the instantaneous physical flow field is studied to find more pieces of evidence for the possible secondary instability mechanisms.

Contours of the absolute value of instantaneous spanwise fluctuation velocity $|w'|$ are exhibited in Figure 15, representing the spanwise fluctuation intensity for four snapshots within one shedding cycle. The K-H roll, labeled with C, forms at station 84%C_{ax} (at $t=t_0-2T_v/3$, not shown in the figure). It sheds downstream, during which this two-dimensional vortex generally becomes three-dimensional and the spanwise fluctuation intensity is amplified more than two orders of magnitude.

In Figure 15(a) and (d), the flow fields at t_0 and t_0+T_v are almost the same, proving that the flow field is periodic in time. In the figures, the hyperbolic instability comes into effect near the saddle point of the hyperbolic streamlines between consecutive K-H rolls. In Figure 15(a) and (d), a strip of local maximum is observed along the stretching direction of the hyperbolic background flow. Preferential growth of u' appears at the same location as marked with a red arrow in Figure 16(a) as well. This peak can be traced back upstream as the hyperbolic streamlines emerge. It moves with the saddle point, during which its intensity is elevated. This local maximum is located exactly on the peak marked with an arrow in Figure 10(a) and (c), suggesting that it is related to the excitation of these modes due to the hyperbolic instability in the braid region.

An arrow is also used in Figure 16(b) to pick out the vortex structures at the exact same location. The local maximum of

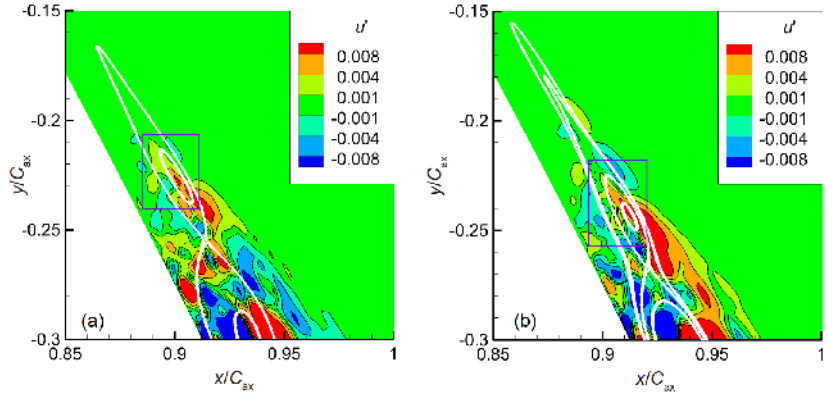

Figure 14 (Color online) Contours of u' amplitudes for mode (1, 6) together with instantaneous streamlines computed from modes (0, 0) and (1, 0). (a) $t=11/16T_v$; (b) $t=7/8T_v$. The vortex core region is marked by the box.

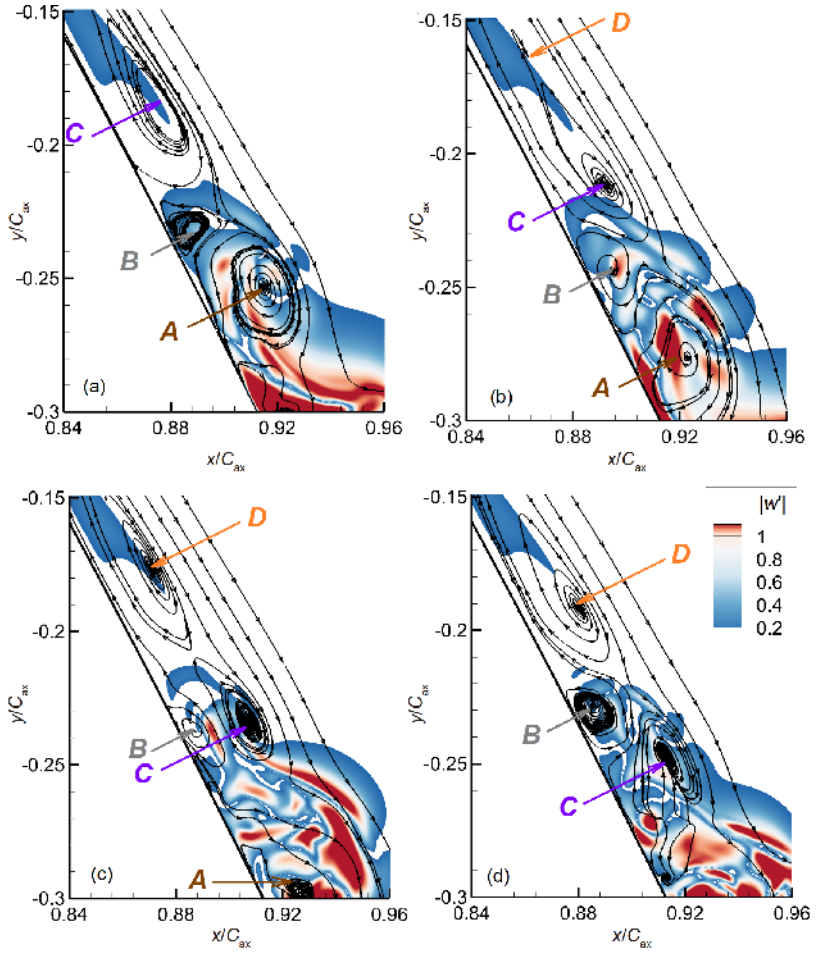

Figure 15 (Color online) Contours of $|w'|$ above 0.01 with streamlines in the x-y cross plane at z=0. (a) t=t_0, (b) t=t_0+T_v/3, (c) t=t_0+2T_v/3, (d) t=t_0+T_v.

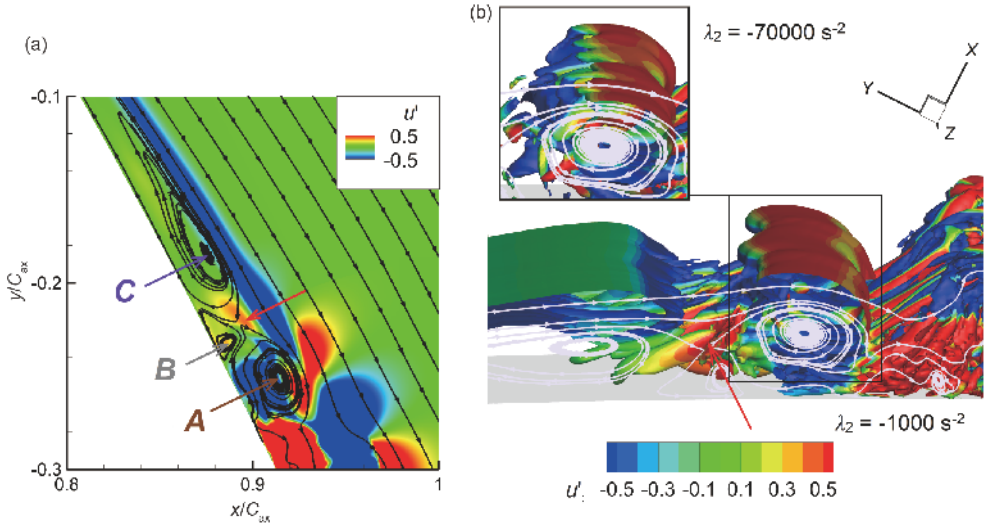

Figure 16 (Color online) The flow field near at t=t_0. (a) Contour of streamwise fluctuation velocity u' in the x-y cross plane at z=0, together with instantaneous streamlines; (b) iso-surfaces of λ_2=−1000 and −70000 s^{-2}, coloured by the streamwise fluctuation velocity u'. λ_2 is a vortex identification [54].

u' is not on the vortex tubes but between a pair of them. Associated with Figure 17(a), we can conjecture that the local maxima of streamwise and spanwise fluctuation velocities are generated by the streamwise vortex tubes. As a pair of streamwise vortices rotate about each other, they sweep the energetic freestream fluid into the near-wall region and

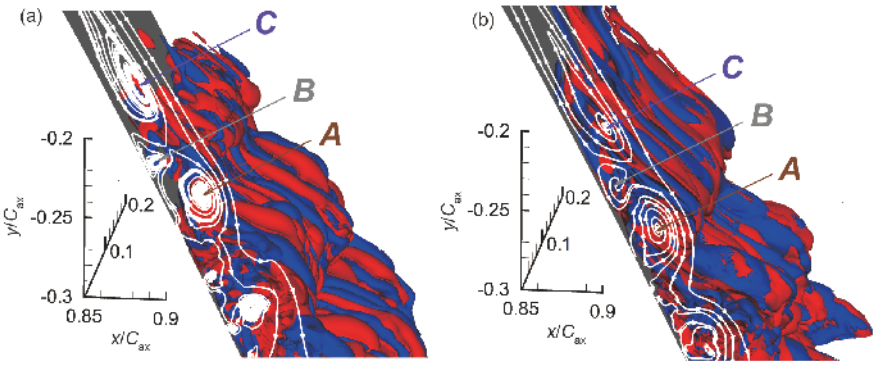

Figure 17 (Color online) Instantaneous iso-surface of streamwise vorticity ω_x= 300 s^{-1} in red and ω_x=−300 s^{-1} in blue with streamlines in the *x*-*y* cross plane at *z*=0 at (a) $t=t_0$; (b) $t=t_0+T_v/3$.

eject the low-speed fluid upward, resulting in local maxima of u' between the pair of vortices and $|w'|$ up the vortices. At $t=t_0$, in Figure 17(a), the streamwise vortices can be found in the braid region between K-H rolls *A* and *C*, while they are absent in the K-H rolls. In Figure 16(b), the K-H roll *C* is still quasi-two-dimension and the K-H roll *A* just presents weak three-dimensional features on its top and in the vortex core at this moment.

If only depends on the streamlines in the *x*-*y* cross plane, one may speculate that the vortex structures just experience a pure translation from $t=t_0$ to $t=t_0+T_v/3$. However, when comparing the streamwise vorticity field in Figure 17(a) and (b), we can find the top of the K-H roll *A* is occupied by the streamwise vortex tubes at $t=t_0+T_v/3$. These streamwise vortex tubes stretch intensely towards not only downstream but also upstream, resulting in the elongated and enhanced strip of $|w'|$ maximum along the "stretching" direction of the hyperbolic background flow in Figure 15(b).

This phenomenon is very similar to the evolution of mode (1, 9) in Figure 13, which is affected strongly by hyperbolic instability. To associate the physical phenomena with oblique modes, Fourier transform in the spanwise direction is conducted in Figure 18 to exhibit the instantaneous spanwise wavenumber of the saddle point and the vortex core. In Figure 18(a), by tracing the saddle point between vortex *C* and *D*, we prove that *k*=3 (or 4) and *k*=9 are the dominant wavenumbers in the braid region. They likely correspond to the aforementioned modes (0.25, 3) and (1, 9), respectively. The fluctuation energy in the braid region increases in both low and high spanwise wavenumber range, which is different from the situation in the vortex core region in Figure 18(b). At $t=t_0+T_v$, the high wavenumber waves are still at a low level in the core of vortex *D*. The peak in the vortex core region is *k*=6, which is likely to refer to the unstable mode (1, 6) discussed in sect. 4.2.

In Marxen et al.'s [24] result, the shear layer possesses a peak-valley character, and the K-H roll is spanwise modulated, corresponding to the elliptical instability of the vortex core. However, a similar phenomenon does not emerge in the current case. In Figure 16(b), the iso-surface of λ_2=−1000 s^{-1} shows that the K-H roll *A* seems spanwise-aligned, with the shear layer above it presenting a spanwise-periodic feature. However, when decreasing the value of λ_2 to −70000 s^{-1} of which the iso-surface can show the vortex core, we can seek out some evidences for elliptical instability. The vortex core

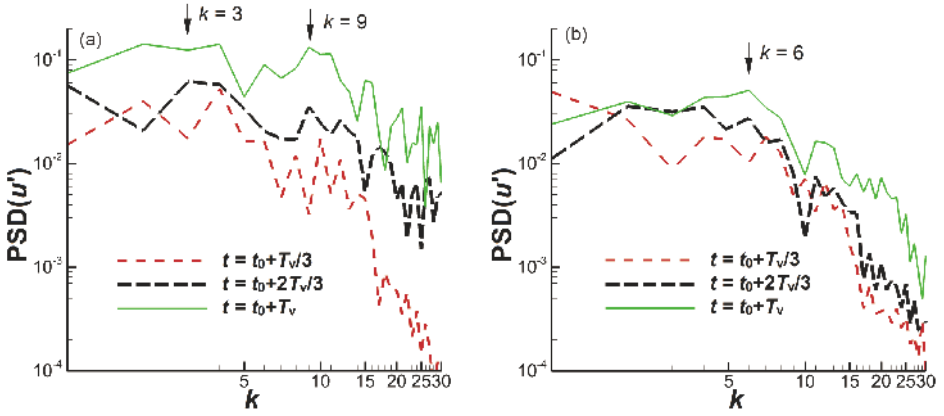

Figure 18 (Color online) PSD of streamwise fluctuation velocity in *z* direction. (a) At the saddle point of the streamline between vortex *C* and *D* in Figure 15(b)-(d); (b) at the vortex core of vortex *D* in Figure 15(b)-(d).

is also spanwise-periodic with a higher wavenumber than the shear layer. The elliptical instability comes into play later than hyperbolic instability. Moreover, It exerts much less influence on the flow field than hyperbolic instability because the spanwise-periodic feature is not so obvious in physical space as the spanwise modulated K-H roll via elliptical instability shown in Figure 7 in ref. [28].

Some local maxima of $|w'|$ are found near-wall, traveling upstream with the reverse flow. These spanwise fluctuations near-wall accelerate the transition process by affecting the bottom of the spanwise vortex *C* as it sheds downstream. Consequently, in Figure 15, the three-dimensionality of vortex *C* starts from the bottom, and the upper part is of negligible $|w'|$ value in the vortex formation region. This process is enhanced when vortex *C* reaches $88\%C_{ax}$, where it encounters the vortex packet *B* directly (see Figure 15(b)). A local maximum of fluctuation intensity is near the interface of vortex *C* and *B*. Surprisingly, this vortex packet *B* does not convect downstream and hovers around $88\%C_{ax}$, keeping interacting with the K-H rolls shedding from upstream. The energy from the downstream flow field can affect the braid region to some extent. As can be seen in Figure 15(b), the vortex packet *B* pumps near-wall spanwise fluctuation energy towards the braid region. Besides, in Figure 15(a), the vortex *A* itself transports small-scale structures to the braid region upstream, similar with Marxen et al.'s [24] result (see Figure 14 in ref. [24])

As shown in Figure 15, despite the existence of mutual interaction between vortex C and *B*, no vortex pairing is observed in this flow field. As declared by McAuliffe and Yaras [16], the presence of pairing was only observed at low Reynolds numbers of about 100, and they also failed to capture pairing instability. The Reynolds number $Re_{\delta 2s}$ based on U_{es} and δ_2 of the current case is 165, still not low enough to see the vortex pairing phenomenon.

6 Summary and concluding remarks

The present work focuses on the origin of three-dimensionality of K-H rolls in the separation-induced transition in a very-low-disturbance environment at a Reynolds number of 5×10^4. The vortex formation and vortex breakup region are investigated in detail, both in Fourier space and physical space, to illustrate the secondary instability mechanisms.

After the shear layer rolls up into a K-H roll, the hyperbolic secondary instability, which is dominant in the current case, is active via elevating the energy for fundamental modes with specific spanwise wavelengths in the braid region. By relating the streamwise vortices to the hyperbolic streamlines, we provide strong evidence for the existence of hyperbolic instability. The streamwise vortices, originating in the braid region, stretch intensely towards both upstream and downstream. They possess spanwise wavelengths in the range centered on 0.2 of the primary streamwise wavelength, which is in accordance with the precedent literatures about the hyperbolic instability. The elliptical instability comes into effect later, responsible for the three-dimensional within the vortex core region. The unstable modes sensitive to elliptical instability possess spanwise wavelengths of about 0.4 of the primary streamwise wavelength.

Nonetheless, some different features are in the current case in comparison with the precedent literatures. Due to the unforced feature of the incoming flow, the modes with a much lower frequency than the fundamental ones are dominant in the vortex formation region. The results also show that some low-frequency modes are also excited in the braid region, which turns out to be the consequences of hyperbolic instability. These works are attempted to improve the current understanding of the secondary instability mechanisms in the separation-induced transition.

Besides the two important secondary instability mechanisms associated with the K-H rolls, there are still two possible instability mechanisms active in the flow field, as discussed in sect. 5. They are the instability in the shear layer and the feedback effect by global instability. More investigations utilizing the stability analysis are needed to provide more evidence for the two mechanisms.

This work is based on a condition with a specific Reynolds number and very low inlet FSTI, under which a short separation bubble forms. It focuses on the instability mechanisms for the laminar separation/ short bubble mode. More numerical and experimental investigations are needed for instability mechanisms of other types of separation-induced transition. They are the laminar separation/long bubble mode under low Reynolds and transitional separation mode in a high-disturbance environment [7].

This work was supported by the National Science and Technology Major Project (Grant No. 2017-II-0004-0016), the National Natural Science Foundation of China (Grant Nos. 11272183, and 11572176), and the National Key Basic Research Program of China (Grant No. 2014CB744801).

1 Z. Yang, Int. J. Comput. Meth. Exp. Meas. **1**, 116 (2013).
2 E. Malkiel, and R. E. Mayle, J. TurboMach. **118**, 752 (1996).
3 T. Michelis, S. Yarusevych, and M. Kotsonis, J. Fluid Mech. **841**, 81 (2018).
4 C. P. Häggmark, A. A. Bakchinov, and P. H. Alfredsson, Philos. Trans. R. Soc. London. Ser. A-Math. Phys. Eng. Sci. **358**, 3193 (2000).
5 U. Rist, and U. Maucher, Eur. J. Mech.-B/Fluids **21**, 495 (2002).
6 M. Talan, and J. Hourmouziadis, Flow Turbul. Combust. **69**, 207 (2002).
7 A. Hatman, and T. Wang, J. TurboMach. **121**, 594 (1999).
8 S. K. Roberts, and M. I. Yaras, J. Fluids Eng. **128**, 232 (2006).
9 S. S. Diwan, and O. N. Ramesh, J. Fluid Mech. **629**, 263 (2009).
10 C. Ho, and P. Huerre, Annu. Rev. Fluid Mech. **16**, 365 (1984).
11 O. Marxen, M. Lang, and U. Rist, J. Fluid Mech. **711**, 1 (2012).
12 J. R. Brinkerhoff, and M. I. Yaras, Phys. Fluids **23**, 124102 (2011).

13 H. Luo, W. Qiao, and K. Xu, J. Therm. Sci. **18**, 193 (2019).
14 J. Dähnert, C. Lyko, and D. Peitsch, J. TurboMach. **135**, (2013).
15 B. R. McAuliffe, and M. I. Yaras, J. TurboMach. **130**, 021006 (2008).
16 B. R. McAuliffe, and M. I. Yaras, J. TurboMach. **132**, 011004 (2010).
17 B. R. McAuliffe, and M. I. Yaras, in *ASME Turbo Expo 2005: Power for Land, Sea, and Air* (American Society of Mechanical Engineers Digital Collection, New York, 2005), pp. 1029-1038.
18 Z. Yang, and P. R. Voke, J. Fluid Mech. **439**, 305 (2001).
19 J. W. Kurelek, A. R. Lambert, and S. Yarusevych, AIAA J. **54**, 2295 (2016).
20 A. Alessandri, P. Bagnerini, M. Gaggero, D. Lengani, and D. Simoni, Phys. Fluids **31**, 044103 (2019).
21 M. S. H. Boutilier, and S. Yarusevych, Phys. Fluids **24**, 084105 (2012).
22 J. Serna, and B. J. Lázaro, Procedia IUTAM **14**, 496 (2015).
23 I. E. Abdalla, and Z. Yang, Int. J. Heat Fluid Flow **25**, 593 (2004).
24 O. Marxen, M. Lang, and U. Rist, J. Fluid Mech. **728**, 58 (2013).
25 J. G. Wissink, and W. Rodi, J. TurboMach. **128**, 668 (2006).
26 A. R. Lambert, and S. Yarusevych, AIAA J. **55**, 2664 (2017).
27 P. R. Spalart, and M. K. Strelets, J. Fluid Mech. **403**, 329 (2000).
28 Z. Yang, and I. E. Abdalla, Comput. Fluids **179**, 595 (2019).
29 M. Gaster, *On the stability of parallel flows and the behaviour of separation bubbles*, Dissertation for the Doctoral Degree (Queen Mary, University of London, London, 1963), pp. 70-72.
30 M. Alam, and N. D. Sandham, J. Fluid Mech. **403**, 223 (2000).
31 M. Embacher, and H. F. Fasel, J. Fluid Mech. **747**, 141 (2014).
32 U. Maucher, U. Rist, and S. Wagner, in *Laminar-Turbulent Transition, Proceedings of the 5th IUTAM Symposium* (Springer, Berlin, 2000), pp. 657-662.
33 D. Barkley, and R. D. Henderson, J. Fluid Mech. **322**, 215 (1996).
34 C. H. K. Williamson, J. Fluid Mech. **328**, 345 (1996).
35 L. E. Jones, R. D. Sandberg, and N. D. Sandham, J. Fluid Mech. **602**, 175 (2008).
36 R. R. Kerswell, Annu. Rev. Fluid Mech. **34**, 83 (2002).
37 V. Theofilis, Annu. Rev. Fluid Mech. **43**, 319 (2011).
38 J. Ren, and S. Fu, Flow Turbulence Combust **94**, 339 (2015).
39 J. Ren, and S. Fu, J. Fluid Mech. **781**, 388 (2015).
40 O. Marxen, M. Lang, U. Rist, O. Levin, and D. S. Henningson, J. Fluid Mech. **634**, 165 (2009).
41 A. Mashayek, and W. R. Peltier, J. Fluid Mech. **708**, 5 (2012).
42 J. H. Huang, *Separation Control over Low Pressure Turbine Blades Using Plasma Actuators*, Dissertation for the Doctoral Degree (University of Notre Dame, Notre Dame, 2005), pp. 24-28.
43 S. Jiang, and S. Fu, Int. Jnl. Num. Meth. HFF **28**, 2208 (2018).
44 B. Yu, W. Q. Tao, J. J. Wei, Y. Kawaguchi, T. Tagawa, and H. Ozoe, Numer. Heat Transfer Part B-Fundamentals **42**, 141 (2002).
45 C. M. Rhie, and W. L. Chow, AIAA J. **21**, 1525 (1983).
46 Y. Kawaguchi, W. Q. Tao, and H. Ozoe, Numer. Heat Transfer Part B-Fundamentals **41**, 85 (2002).
47 Q. J. Wang, Y. X. Ren, Z. S. Sun, and Y. T. Sun, Sci. China-Phys. Mech. Astron. **56**, 423 (2013).
48 D. Rizzetta, and M. Visbal, "*Numerical investigation of transitional flow through a low-pressure turbine cascade*", AIAA Paper No. 2003-3587, 2003.
49 F. R. Menter, R. Langtry, and S. Völker, Flow Turbul. Combust. **77**, 277 (2006).
50 L. Wang, and S. Fu, Sci. China Ser. G-Phys. Mech. Astron. **52**, 768 (2009).
51 L. Wang, S. Fu, A. Carnarius, C. Mockett, and F. Thiele, Int. J. Heat Fluid Flow **34**, 62 (2012).
52 S. Poondru, *Large-eddy Simulation and Active Flow Control of Low-Reynolds Number Flow Through A Low-Pressure Turbine Cascade*, Dissertation for the Doctoral Degree (University of Cincinnati, Cincinnati, 2008), pp. 90-109.
53 C. P. Caulfield, and R. R. Kerswell, Phys. Fluids **12**, 1032 (2000).
54 J. Jeong, and F. Hussain, J. Fluid Mech. **285**, 69 (1995).